



**Small Molecule-Induced Allosteric Activation of the  
Vibrio cholerae RTX Cysteine Protease Domain**

Patrick J. Lupardus, *et al.*

*Science* **322**, 265 (2008);

DOI: 10.1126/science.1162403

***The following resources related to this article are available online at  
www.sciencemag.org (this information is current as of October 12, 2008 ):***

**Updated information and services**, including high-resolution figures, can be found in the online version of this article at:

<http://www.sciencemag.org/cgi/content/full/322/5899/265>

**Supporting Online Material** can be found at:

<http://www.sciencemag.org/cgi/content/full/322/5899/265/DC1>

This article **cites 13 articles**, 8 of which can be accessed for free:

<http://www.sciencemag.org/cgi/content/full/322/5899/265#otherarticles>

This article appears in the following **subject collections**:

Biochemistry

<http://www.sciencemag.org/cgi/collection/biochem>

Information about obtaining **reprints** of this article or about obtaining **permission to reproduce this article** in whole or in part can be found at:

<http://www.sciencemag.org/about/permissions.dtl>

# Small Molecule–Induced Allosteric Activation of the *Vibrio cholerae* RTX Cysteine Protease Domain

Patrick J. Lupardus,<sup>1\*</sup> Aimee Shen,<sup>3\*</sup> Matthew Bogoy,<sup>3†</sup> K. Christopher Garcia<sup>1,2†</sup>

*Vibrio cholerae* RTX (repeats in toxin) is an actin-disrupting toxin that is autoprocessed by an internal cysteine protease domain (CPD). The RTX CPD is efficiently activated by the eukaryote-specific small molecule inositol hexakisphosphate (InsP<sub>6</sub>), and we present the 2.1 angstrom structure of the RTX CPD in complex with InsP<sub>6</sub>. InsP<sub>6</sub> binds to a conserved basic cleft that is distant from the protease active site. Biochemical and kinetic analyses of CPD mutants indicate that InsP<sub>6</sub> binding induces an allosteric switch that leads to the autoprocessing and intracellular release of toxin-effector domains.

Most secreted bacterial toxins are produced as inactive precursors that become proteolytically activated upon entering a eukaryotic cell (1). A select group of these toxins undergo autoproteolysis upon entry into the host cytosol, resulting in the release of their effector domains (2, 3). The *Vibrio cholerae* RTX (repeats in toxin) is a member of the multifunctional autoprocessing RTX (MARTX) family of toxins, which all contain a cysteine protease domain (CPD) predicted to mediate the autoproteolytic activation of the secreted protoxin upon entry into the eukaryotic cytosol (4). Almost all clinical and environmental isolates of *V. cholerae* produce RTX (5), which enhances virulence and

colonization in murine models of *V. cholerae* infection (6, 7). RTX autoprocessing is thought to release its actin-disrupting effector domains from the target cell's plasma membrane into the cytosol (4) (fig. S1). Although autoproteolysis is essential for RTX toxin function (3), the mechanism of RTX CPD activation is unclear.

It has recently been shown that the small molecules guanosine 5'-triphosphate (GTP) and inositol hexakisphosphate (InsP<sub>6</sub>) stimulate autoprocessing of the RTX CPD (3, 8); also, InsP<sub>6</sub> activates a distantly related protease domain in toxin B of *Clostridium difficile* (2, 9). We tested the ability of guanosine 5'-O-(3'-thiotriphosphate) (GTP-γ-S), InsP<sub>6</sub>, and InsP<sub>6</sub> metabolites to ac-

tivate *V. cholerae* RTX CPD autocleavage in vitro. InsP<sub>6</sub> potently activated autocatalysis, with a half-maximal autocleavage concentration (AC<sub>50</sub>) of 0.9 nM versus 0.19 μM, 0.72 μM, and 240 μM for InsP(1,4,5,6)<sub>4</sub>, InsP(1,3,4,5,6)<sub>5</sub>, and GTP-γ-S, respectively (Fig. 1A and fig. S3). We confirmed the interaction between InsP<sub>6</sub> and RTX CPD using surface plasmon resonance (SPR), which indicated that InsP<sub>6</sub> binds to the RTX CPD with an equilibrium binding affinity constant (K<sub>d</sub>) of 1.3 ± 0.2 μM (Fig. 1B).

To gain structural insight into the InsP<sub>6</sub>-mediated activation of RTX CPD, we purified an autocleaved minimal RTX CPD catalytic domain for cocrystallization with InsP<sub>6</sub> (10). We determined the structure of the RTX CPD at a resolution of 2.1 Å, consisting of amino acids 5 through 203 (with residue 1 being the P1' alanine and P1' referring to the residue C-terminal to the scissile bond). The protease domain comprises a seven-stranded beta sheet, with five central parallel strands and two antiparallel capping strands (Fig. 1, C and D). Two helices flank one

**Fig. 1.** InsP<sub>6</sub> activates the *V. cholerae* RTX CPD and the architecture of the InsP<sub>6</sub>-CPD complex. (A) Activation of RTX cysteine protease domain autocleavage by InsP<sub>6</sub>. Recombinant RTX CPD (amino acids 3391 to 3650) was incubated with the indicated concentrations of InsP<sub>6</sub> for 2 hours, and autocleavage was assessed by SDS–polyacrylamide gel electrophoresis (SDS–PAGE) and Coomassie staining (representative gel inset). Reactions were performed in triplicate, and the amount of autocleaved protein relative to the total protein amount was analyzed by densitometry, averaged and plotted versus concentration of InsP<sub>6</sub>. 50% of the wild-type CPD was autoprocessed (AC<sub>50</sub>) at 0.85 ± 0.02 nM InsP<sub>6</sub> (mean ± SD). (B) SPR analysis of InsP<sub>6</sub> binding to wild-type biotinylated CPD immobilized on a streptavidin-coupled surface. Representative sensorgram (inset) shows the binding of InsP<sub>6</sub> to the CPD-bound surface over a concentration of 0.1 to 100 μM. Equilibrium binding analysis indicates a K<sub>d</sub> of 1.3 ± 0.2 μM (SD). (C) Structure of the CPD–InsP<sub>6</sub> complex viewed from above the InsP<sub>6</sub>-binding site. (D) A view of the structure rotated ~135° to show the active site. The InsP<sub>6</sub>-binding and active sites are separated by a 22-amino acid β-hairpin structure (β-flap). InsP<sub>6</sub> and the side chains of the catalytic dyad (Cys140/His91) are shown as stick models.

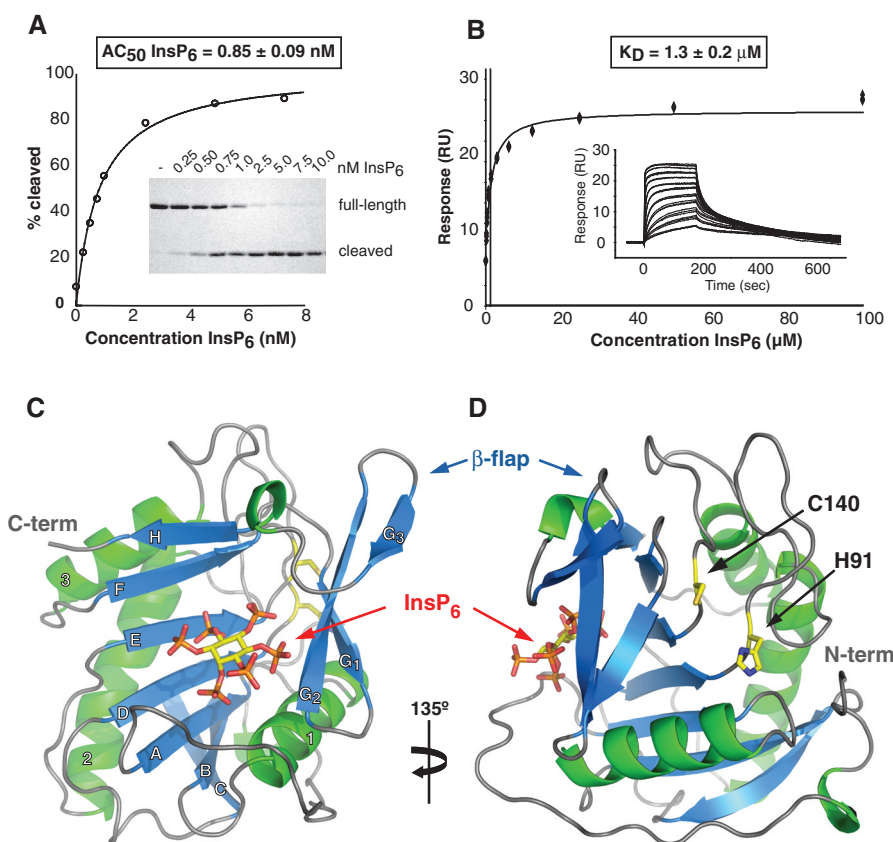


**Fig. 2.** The  $\text{InsP}_6$ -binding and active sites. **(A)** Electrostatic surface potential of the CPD as viewed from above the  $\text{InsP}_6$ -binding site. Blue denotes a positively charged surface; red denotes a negatively charged surface.  $\text{InsP}_6$  is shown in the binding site as a stick model. **(B)** Close-up view of the  $\text{InsP}_6$ -binding site. Side chains that directly interact with  $\text{InsP}_6$  are labeled and shown as yellow sticks. The electron density for  $\text{InsP}_6$  ( $2F_{\text{obs}} - F_{\text{calc}}$ ) is contoured at  $2\sigma$ . **(C)** Surface topology of the CPD active site. The P1 substrate pocket, C140, and H91 are highlighted in orange, yellow, and blue, respectively. The N terminus is shown as a yellow ribbon, terminating at Ile5 and highlighting the threading of this region along the surface of the core domain. The remaining residues not visible at the N terminus are depicted as a yellow dashed line to illustrate the approximate positioning of the chain during catalysis. **(D)** Close-up view of the P1 substrate pocket. Amino acids that line the pocket are labeled and colored orange.  $\text{InsP}_6$  is shown as in (B) to demonstrate the position of the catalytic site with respect to the  $\text{InsP}_6$ -binding site.

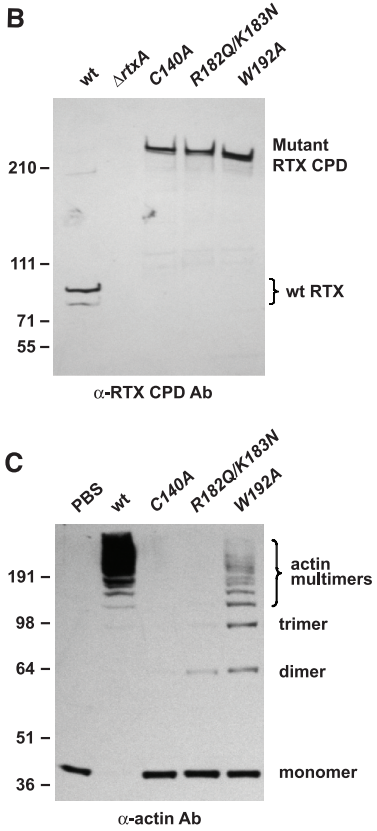
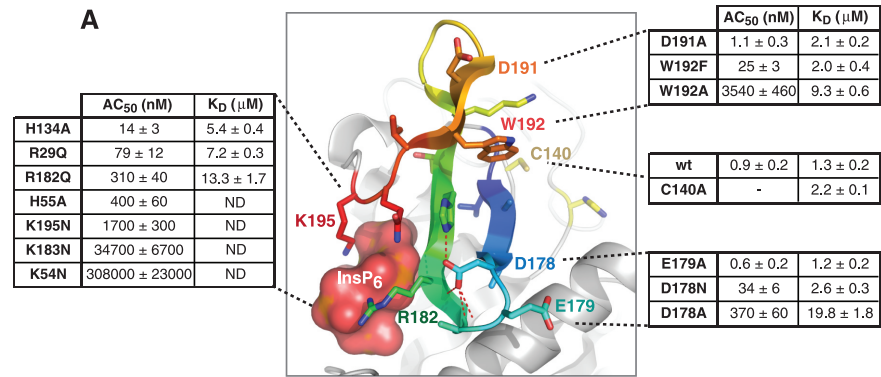
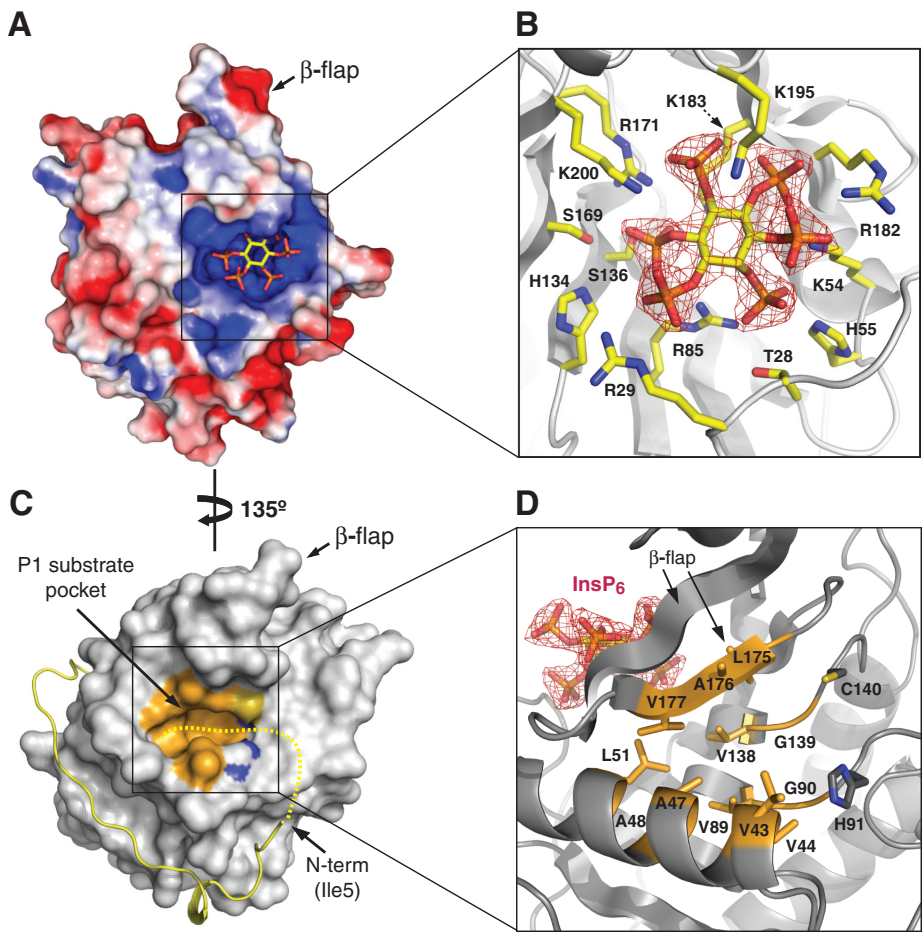


**Fig. 3.**  $\beta$ -Flap mutations decouple CPD autocatalysis and RTX activity from  $\text{InsP}_6$  binding. **(A)** Comparison of autocleavage efficiency ( $AC_{50}$ ) versus  $\text{InsP}_6$  binding ( $K_D$ ) measured by SPR for mutations in the  $\text{InsP}_6$ -binding site (left table) and  $\beta$ -flap (right tables, top and bottom). The  $\beta$ -flap region of the CPD is rainbow-colored, starting with blue at the N-terminal end. The  $\beta$ -flap, catalytic site, and visible  $\text{InsP}_6$ -interacting side chains are shown as sticks. Data are expressed as mean  $\pm$  SD. ND, not determinable. **(B)** Western blot analysis of RTX in supernatant harvested from log-phase *V. cholerae* cultures. Supernatants from *V. cholerae* strains harboring either an intact *rtxA* gene (wt), a null mutation in *rtxA* ( $\Delta$ *rtxA*), or point mutations in the region encoding the CPD domain of RTX (C140A is catalytic-dead; R182Q/K183N is mutated at two  $\text{InsP}_6$ -binding residues; and W192A is a  $\beta$ -flap mutation) were blotted using an anti-CPD antibody. **(C)** Actin crosslinking induced upon incubation of *V. cholerae* with HFF cells. *V. cholerae* strains used in (A) were incubated with HFFs for 90 min, then the HFF cells were lysed. Actin crosslinking was visualized by SDS-PAGE and Western blotting by using an actin-specific antibody. The crosslinked forms of actin are labeled to the right.



side of the sheet, lying diagonally in a groove created by a  $\sim 90^\circ$  twist of the sheet, and a third helix caps the other side of the sheet. The Cys-His catalytic dyad (C140 and H91) lies at the C-terminal ends of the central D and E  $\beta$  strands. The overall structure is reminiscent of the clan CD family of cysteine proteases, which suggests a common ancestor for this family of enzymes. Comparison with the two most closely related known protease structures, human caspase-7 (11) and *Porphyromonas gingivalis* gingipain-R (12) (fig. S4), reveals that two C-terminal helices have been replaced by a three-strand flap. This “ $\beta$ -flap” structure forms a cleft in which we identified electron density for a single InsP<sub>6</sub> molecule (fig. S5).

The InsP<sub>6</sub>-binding pocket is lined with basic residues, burying approximately 890 Å<sup>2</sup> of surface area (Fig. 2A). Nine of the twelve residues that directly interact with InsP<sub>6</sub> via hydrogen bond contacts are positively charged, with a core of six residues (K54, R85, S136, R171, K183, and K200) forming the bottom of the pocket and five others surrounding the InsP<sub>6</sub> molecule (T28, R29, H55, H134, S169, and R182) (Fig. 2B and fig. S6) (13). K195 covers the top of the InsP<sub>6</sub> molecule, interacting with the C1, C5, and C6 phosphate groups. The protein-InsP<sub>6</sub> interface is further stabilized by a network of water molecules between InsP<sub>6</sub> and the  $\beta$ -flap. On the opposite side of the  $\beta$ -flap is the catalytic dyad and a large hydrophobic pocket for the P1 amino acid (the residue N-terminal to the scissile bond) (Fig. 2C). The  $\beta$ -flap contributes three of the twelve hydrophobic amino acids that line one side of the P1 pocket, and helix 1 and two central beta sheets (D and E) contribute the remainder (Fig. 2D). The surface properties and size of the P1 substrate pocket are consistent with the cleavage of RTX CPD after an N-terminal leucine (3). The final N-terminal residue observed in our structure is I5 (the P5' position) (Fig. 2C), which lies  $\sim 14$  Å from the catalytic cysteine. No electron density was observed for the P1' through P4' positions, suggesting that they do not make strong contacts with the protease and may minimally contribute to substrate specificity.

The InsP<sub>6</sub>-binding site is structurally segregated from the active site, which clearly indicates that InsP<sub>6</sub> does not act as a cofactor for catalysis. Indeed, kinetic analyses revealed that InsP<sub>6</sub> binding is independent of substrate binding to the active site and that the concentration of InsP<sub>6</sub> does not alter the affinity of the InsP<sub>6</sub>-bound enzyme for its substrate (fig. S7). Because RTX CPD activity was strictly dependent on InsP<sub>6</sub> in these analyses, we hypothesized that InsP<sub>6</sub> binding may regulate exposure of the active site. We therefore tested the ability of a fluorescent maleimide derivative to alkylate the catalytic cysteine of wild-type CPD and a mutant CPD lacking two InsP<sub>6</sub>-interacting residues (R182Q/K183N) (14). Although weak fluorescent labeling was observed for both wild-type and mutant CPD in the absence of InsP<sub>6</sub>, dose-

dependent labeling of the active-site cysteine was observed in the presence of InsP<sub>6</sub> only for the wild-type CPD (fig. S8). Thus, productive binding of InsP<sub>6</sub> is required to expose the active-site cysteine of the protease to substrates and inhibitors. Consistent with this observation, pretreatment of wild-type CPD immobilized on an SPR chip with *N*-ethylmaleimide (NEM) alone failed to block InsP<sub>6</sub>-induced autocleavage of the CPD from the chip (fig. S9). Simultaneous treatment of the CPD with InsP<sub>6</sub> and NEM, however, inhibited InsP<sub>6</sub>-induced autocleavage, which indicated that NEM can only react with the active-site cysteine in the presence of InsP<sub>6</sub>. These results strongly suggest an allosteric mechanism of activation in which the active site is disordered or occluded in the absence of InsP<sub>6</sub>, a mode of regulation that likely protects the protease active-site sulfhydryl until the toxin enters a eukaryotic cell.

Inspection of the structure suggested that the  $\beta$ -flap, which lines the side of the InsP<sub>6</sub>-binding cleft closest to the catalytic site, may contribute to enzyme activation by properly ordering the P1 pocket and active site. Among the many side chains that coordinate InsP<sub>6</sub>, the  $\beta$ -flap contains three residues (R182, K183, and K195) that form a three-pronged “clamp” above and below InsP<sub>6</sub> (Figs. 2A and 3A). We tested the effect of the mutations R182Q, K183N, and K195N on both InsP<sub>6</sub> binding (fig. S10) and catalytic activity (fig. S11) relative to wild-type CPD (Fig. 3A). Mutation of K183 and K195 abrogated both InsP<sub>6</sub> binding and autocleavage activity (Fig. 3A, left table), whereas mutation of R182 only moderately reduced InsP<sub>6</sub> binding but dramatically decreased autocatalysis as compared with the wild type. R182 not only binds InsP<sub>6</sub>, it also engages in structurally stabilizing hydrogen-bonding interactions with D24 (fig. S12). This may explain the more considerable impact of the R182Q mutation on catalysis rather than InsP<sub>6</sub> binding, because R182 may primarily fine-tune the structure of the  $\beta$ -flap and may contribute nominally to binding InsP<sub>6</sub>. Thus, diminution of InsP<sub>6</sub> binding on one side of the flap clearly reduces catalysis mediated by residues on the opposite side of the flap.

We sought to determine if the mutation of non-InsP<sub>6</sub>-interacting residues in the  $\beta$ -flap might “decouple” InsP<sub>6</sub>-binding affinity from the autocatalytic activity of the enzyme. We focused on W192 in strand G<sub>3</sub>, which makes van der Waals contacts with strands G<sub>1</sub> and G<sub>2</sub> (Fig. 3A), and D178, which stabilizes the G<sub>1</sub>-G<sub>2</sub>  $\beta$ -hairpin by hydrogen bonding with three backbone amide nitrogens and helps anchor the center of the G<sub>2</sub> strand by forming a salt bridge with the side chain of H184 (Fig. 3A). We made conservative (W192F and D178N) and more potent (W192A and D178A) mutations; as controls, we also mutated nearby solvent-facing residues D191 and E179 (D191A and E179A). The conservative mutations (W192F and D178N) minimally altered InsP<sub>6</sub>-binding affinity yet considerably reduced autocatalysis relative to the wild type and controls D191A and E179A (Fig. 3A, right). Fur-

thermore, the more potent W192A and D178A mutations induced only a modest drop in InsP<sub>6</sub>-binding affinity yet a more severe defect in catalysis. The D178A mutant exhibited InsP<sub>6</sub> binding and catalytic activity similar to those of the R182Q mutant, consistent with their similar positions in the  $\beta$ -flap. The W192A mutant was most dramatically affected; despite having moderate affinity for InsP<sub>6</sub> ( $9.3 \pm 0.6$   $\mu$ M), W192A had a catalytic defect that was twice as strong as that of the InsP<sub>6</sub>-binding mutant K195N. Thus, mutation of residues that apparently communicate InsP<sub>6</sub> binding to the active site through structural rearrangement of the  $\beta$ -flap can decouple InsP<sub>6</sub> binding from enzyme activation. The proposed structural rearrangement, however, appears to be subtle because the circular dichroism (CD) spectra of the free- and InsP<sub>6</sub>-bound enzymes were nearly superimposable (fig. S13).

To assess the biological importance of InsP<sub>6</sub> binding and  $\beta$ -flap integrity on RTX CPD function in vivo, we constructed *V. cholerae* strains containing CPD point mutations C140A (catalytic dead), R182Q/K183N (InsP<sub>6</sub>-binding defective), and W192A ( $\beta$ -flap-transition defective). Western detection of the CPD (Fig. 3B) showed that although most wild-type RTX was autoprocessed during the growth of *V. cholerae* in LB medium, RTX containing catalytic dead (C140A), InsP<sub>6</sub>-binding (R182Q/K183N), or  $\beta$ -flap (W192A) mutations were unprocessed (Fig. 3B). Thus, even in the presence of high levels of InsP<sub>6</sub> in LB medium, all three mutations prevented CPD activation in the native RTX. When *V. cholerae* mutant strains or supernatants were incubated with human foreskin fibroblast (HFF) cells, intracellular actin cross-linking induced by the mutant strains R182Q/K183N and W192A was severely reduced relative to the wild type, whereas C140A failed to induce actin cross-linking (Fig. 3C and fig. S14). Thus, InsP<sub>6</sub> binding and an intact  $\beta$ -flap are required for RTX autocleavage and effector function.

The InsP<sub>6</sub>-interacting residues in related MARTX cysteine protease domains are almost invariably conserved (fig. S2), which strongly suggests a shared mechanism for toxin activation in Gram-negative bacteria. Because InsP<sub>6</sub> is exclusive to eukaryotes (15) and is present at cytosolic concentrations  $>10$   $\mu$ M (16), the responsiveness of the MARTX family to InsP<sub>6</sub> through the evolution of a proteolytic biosensor seems an ingenious strategy for regulating the function of a secreted toxin.

#### References and Notes

1. V. M. Gordon, S. H. Leppla, *Infect. Immun.* **62**, 333 (1994).
2. J. Reineke *et al.*, *Nature* **446**, 415 (2007).
3. K. L. Sheahan, C. L. Cordero, K. J. Satchell, *EMBO J.* **26**, 2552 (2007).
4. K. J. Satchell, *Infect. Immun.* **75**, 5079 (2007).
5. C. L. Cordero, S. Sozhamannan, K. J. Satchell, *J. Clin. Microbiol.* **45**, 2289 (2007).
6. V. Olivier, G. K. Haines 3rd, Y. Tan, K. J. Satchell, *Infect. Immun.* **75**, 5035 (2007).
7. V. Olivier, N. H. Salzman, K. J. Satchell, *Infect. Immun.* **75**, 5043 (2007).
8. K. Prochazkova, K. J. Satchell, *J. Biol. Chem.* **283**, 23656 (2008).

9. M. Egerer, T. Giesemann, T. Jank, K. J. Satchell, K. Aktories, *J. Biol. Chem.* **282**, 25314 (2007).

10. Materials and methods are available as supporting material on Science Online.

11. J. A. Hardy, J. Lam, J. T. Nguyen, T. O'Brien, J. A. Wells, *Proc. Natl. Acad. Sci. U.S.A.* **101**, 12461 (2004).

12. A. Eichinger et al., *EMBO J.* **18**, 5453 (1999).

13. Single-letter abbreviations for the amino acid residues are as follows: A, Ala; C, Cys; D, Asp; E, Glu; F, Phe; G, Gly; H, His; I, Ile; K, Lys; L, Leu; M, Met; N, Asn; P, Pro; Q, Gln; R, Arg; S, Ser; T, Thr; V, Val; W, Trp; and Y, Tyr.

14. In the mutants, other amino acids were substituted at certain locations; for example, R182Q indicates that arginine at position 182 was replaced by glutamine.

15. R. H. Michell, *Nat. Rev. Mol. Cell Biol.* **9**, 151 (2008).

16. R. F. Irvine, M. J. Schell, *Nat. Rev. Mol. Cell Biol.* **2**, 327 (2001).

17. We thank S. Juo for assistance with data collection and structure determination, E. D. Sandoval for assistance with kinetic analyses and helpful discussion, M. Blokech and G. Schoolnik for help with *V. cholerae* strain construction, and A. Guzzetta for intact mass analysis of SeMet-labeled CPD. P.J.L. is a Damon Runyon Fellow, supported by the Damon Runyon Cancer Research Foundation. K.C.G. is supported by the NIH Keck Foundation and the Howard Hughes Medical Institute. M.B. is supported by the Burroughs Wellcome Foundation, the Searle Scholars Program, and the NIH National Technology Center for Networks and Pathways (grant U54RR020843). P.J.L., A.S., M.B., and K.C.G. are listed

as inventors on a patent application related to use of the *V. cholerae* RTX CPD for biotechnical applications. Coordinates and structure factors have been deposited in the Protein Data Bank ([www.rcsb.org](http://www.rcsb.org)) under accession number 3EEB.

**Supporting Online Material**  
[www.sciencemag.org/cgi/content/full/322/5899/265/DC1](http://www.sciencemag.org/cgi/content/full/322/5899/265/DC1)  
Materials and Methods  
Figs. S1 to S14  
Tables S1 to S3  
References

26 June 2008; accepted 10 September 2008  
10.1126/science.1162403

# Noncytotoxic Lytic Granule–Mediated CD8<sup>+</sup> T Cell Inhibition of HSV-1 Reactivation from Neuronal Latency

Jared E. Knickelbein,<sup>1,2,3</sup> Kamal M. Khanna,<sup>3\*</sup> Michael B. Yee,<sup>3</sup> Catherine J. Baty,<sup>4,5</sup> Paul R. Kinchington,<sup>3,6</sup> Robert L. Hendricks<sup>3,6,7†</sup>

Reactivation of herpes simplex virus type 1 (HSV-1) from neuronal latency is a common and potentially devastating cause of disease worldwide. CD8<sup>+</sup> T cells can completely inhibit HSV reactivation in mice, with interferon- $\gamma$  affording a portion of this protection. We found that CD8<sup>+</sup> T cell lytic granules are also required for the maintenance of neuronal latency both in vivo and in ex vivo ganglia cultures and that their directed release to the junction with neurons in latently infected ganglia did not induce neuronal apoptosis. Here, we describe a nonlethal mechanism of viral inactivation in which the lytic granule component, granzyme B, degrades the HSV-1 immediate early protein, ICP4, which is essential for further viral gene expression.

Several lines of evidence support a role for CD8<sup>+</sup> T cells in controlling herpes simplex virus type 1 (HSV-1) latency. CD8<sup>+</sup> T cells, many expressing granzyme B (GrB), are found juxtaposed to HSV-1 latently infected sensory neurons of both humans (1–4) and mice (5–8). In C57BL/6 mice, CD8<sup>+</sup> T cells specific for the immunodominant HSV-1 glycoprotein B<sub>498–505</sub> epitope (gB-CD8) polarize their T cell receptor (TCR) to junctions with neurons in situ forming apparent immunologic synapses (9). Murine gB-CD8 can block HSV-1 reactivation from latency in vivo and in ex vivo ganglia cultures in a major histocompatibility complex–dependent manner (9–11). Because HSV-1 estab-

lishes latency solely within ganglionic neurons (12, 13), we hypothesize that some latently infected neurons directly present viral antigens to HSV-specific CD8<sup>+</sup> T cells during attempted reactivation, which is subsequently quelled by CD8<sup>+</sup> T cell effector functions.

CD8<sup>+</sup> T cells can use interferon- $\gamma$  (IFN- $\gamma$ ) to block HSV-1 reactivation in some, but not all, latently infected sensory neurons (14, 15). HSV-1 reactivation is suppressed by CD8<sup>+</sup> T cells in neurons that are refractory to IFN- $\gamma$  through an as yet undefined mechanism. Lytic granules represent an important CD8<sup>+</sup> T cell effector mechanism, but their use is generally lethal to targeted cells. GrB-expressing gB-CD8 from latently infected trigeminal ganglia (TG) polarized and released their lytic granules toward susceptible fibroblasts, leading to apoptosis (fig. S1) (16). Thus, we investigated whether gB-CD8 used lytic granules during immunosurveillance of latently infected neurons and also whether they induced neuronal apoptosis.

GrB<sup>+</sup> gB-CD8 expanded from latently infected TG of wild-type (WT) mice (fig. S2) were added to cultures of dispersed TG in which reactivated HSV-1 had spread to the surrounding fibroblasts. Most fibroblasts targeted by gB-CD8 showed active caspase staining in punctate, multifocal, or diffuse patterns (fig. S3, A and C), which is consistent with early, intermediate, and late stages of apoptosis, respectively (17). Conversely, none of the gB-CD8–targeted neurons showed

caspase activation (fig. S3, B and C). Thus, either CD8<sup>+</sup> T cells do not release lytic granules toward neurons, or lytic granule release does not activate the caspase system of neurons.

To distinguish between these possibilities, we first documented CD8<sup>+</sup> T cell polarization of GrB toward junctions with neurons in latently infected TG in situ (Fig. 1A) and ex vivo (Fig. 1B), suggesting ongoing use of directed lytic granule release by CD8<sup>+</sup> T cells during immunosurveillance of latently infected ganglia. Histologic studies of HSV-1 latently infected human (1–4) and murine (5–8) ganglia have failed to detect morphologic signs of apoptosis in neurons in direct contact with activated CD8<sup>+</sup> T cells. To directly investigate whether neurons are refractory to lytic granule-mediated apoptosis, WT GrB-expressing gB-CD8 were added to dispersed latently infected TG directly ex vivo when HSV-1 is confined to neurons. Of 13 documented neuron/CD8<sup>+</sup> T cell interactions exhibiting lytic granule release, none of the targeted neurons exhibited activated caspases (Fig. 1C), whereas neuronal caspases could be activated by ethanol treatment (Fig. 1D). CD8<sup>+</sup> T cells contacting nonneuronal cells or not contacting any cell showed no lytic granule release (Fig. 1E). The selective resistance of neurons to apoptosis induction by CD8<sup>+</sup> T cell lytic granules might be

**Table 1.** Pfn<sup>−/−</sup> and GrB<sup>−/−</sup> gB-CD8 are less efficient than WT gB-CD8 at inhibiting HSV-1 reactivation in a common pool of latently infected neurons. HSV-1 reactivation detected by plaque assay of supernatants from dispersed 34- to 44-dpi WT TG depleted of endogenous CD8<sup>+</sup> T cells and cultured at one-fifth TG per well with the indicated number and type of gB-CD8 from culture initiation. +, reactivation detected; −, no reactivation detected; x, condition not tested. Data were pooled from four independent experiments (n = 15 to 35 cultures per condition).

Number of gB-CD8 per well	Type of gB-CD8		
	WT	Pfn <sup>−/−</sup>	GrB <sup>−/−</sup>
2 × 10 <sup>3</sup>	+	x	x
2 × 10 <sup>4</sup>	−	+	+
4 × 10 <sup>4</sup>	−	+	+
5 × 10 <sup>4</sup>	−	+	−
1 × 10 <sup>5</sup>	−	+	−

<sup>1</sup>Graduate Program in Immunology, University of Pittsburgh School of Medicine, Pittsburgh, PA 15213, USA. <sup>2</sup>Medical Scientist Training Program, University of Pittsburgh School of Medicine, Pittsburgh, PA 15213, USA. <sup>3</sup>Department of Ophthalmology, University of Pittsburgh School of Medicine, Pittsburgh, PA 15213, USA. <sup>4</sup>Center for Biologic Imaging, University of Pittsburgh School of Medicine, Pittsburgh, PA 15213, USA. <sup>5</sup>Department of Cell Biology and Physiology, University of Pittsburgh School of Medicine, Pittsburgh, PA 15213, USA. <sup>6</sup>Department of Microbiology and Molecular Genetics, University of Pittsburgh School of Medicine, Pittsburgh, PA 15213, USA. <sup>7</sup>Department of Immunology, University of Pittsburgh School of Medicine, Pittsburgh, PA 15213, USA.

\*Present address: Department of Immunology, University of Connecticut, Farmington, CT 06030, USA.

†To whom correspondence should be addressed. E-mail: [hendricksrr@upmc.edu](mailto:hendricksrr@upmc.edu)